energies

MDPI

Article

Development of a Simulation Model for a New Rotary Engine to Optimize Port Location and Operating Conditions Using GT-POWER

Young-Jic Kim, Young-Joon Park, Tae-Joon Park and Chang-Eon Lee *

Department of Mechanical Engineering, Inha University, Incheon 22212, Republic of Korea; bokyjkim@inha.edu (Y.-J.K.); youngjoon.park@inha.edu (Y.-J.P.); ptj@inha.edu (T.-J.P.)
* Correspondence: chelee@inha.ac.kr

Abstract: The objective of this study is to develop a 1D CFD simulation model to identify the optimal design parameters, using GT-POWER prior to the optimization of a new rotary engine derived from a three-lobe gerotor pump (GP3 RTE) based on 3D CFD simulation. The models were compared based on their respective development stages (steps 1–4) to ascertain the impact of each parameter on performance. The step 4 model, which exhibited a similar trend to that observed in the 3D CFD results, was selected for further analysis and validation. The developed model accurately predicted GP3 RTE performance in terms of fuel consumption, indicated power, efficiency, and exhaust gas reticulation (EGR) behavior, approaching the accuracy of the CONVERGE model. Furthermore, the optimal intake/exhaust port locations and operating conditions of the GP3 RTE were derived using the developed step 4 model. The model provided a convenient and powerful tool for obtaining basic information regarding the unique behavior of the GP3 RTE, thereby enabling the optimization of the design parameters without the necessity for time-consuming three-dimensional design modifications.

Keywords: new rotary engine; gerotor pump; EGR; virtual reciprocating engine; one-dimensional CFD model

Citation: Kim, Y.-J.; Park, Y.-J.; Park, T.-J.; Lee, C.-E. Development of a Simulation Model for a New Rotary Engine to Optimize Port Location and Operating Conditions Using GT-POWER. *Energies* **2024**, *17*, 4732. https://doi.org/10.3390/en17184732

Academic Editor: Jianbing Gao

Received: 5 August 2024
Revised: 2 September 2024
Accepted: 5 September 2024
Published: 23 September 2024

1. Introduction

Rotary engines (RTEs) do not require a crank mechanism and have simple intake and exhaust systems and hence require a considerably lower number of engine parts compared with reciprocating engines (REs), which is particularly advantageous for special purpose engines. The Wankel engine (WE) is a fairly typical RTE developed in the early 1960s [1], and RTEs based on the WE design provide several advantages and disadvantages. The advantages include simple structure, low friction loss, and high power output relative to the engine weight, providing relatively high-speed rotation with low vibration and torque fluctuations, whereas the disadvantages include poor fuel economy and emission performance, a complex sealing and lubrication system, and poor durability. These latter shortcomings can be attributed to the WE's underlying structural characteristics: the WE combustion chamber has to be installed on the inner rotor, requiring the shape to be a thin rectangle, and combustion must occur in a rotating space, which also requires pressure seals to prevent leakage to be located on the inner rotor surface, with some difficulties in ensuring adequate lubrication [2–8].

LiquidPiston recently developed an X engine (XE), basically reversing the WE shape [9] and employing two rotor lobes in a gerotor pump-shaped housing with three lobes, compared to the WE, which requires two lobes for the housing. Thus, the XE combustion chamber can be installed in a fixed housing and has relatively loose shape design criteria. In particular, the XE's sealing and lubrication position reduce gas leakage problems because it largely employs a fixed housing [10]. The XE's operation and basic principles were verified during its early development for a water-cooled 70 HP-class diesel engine [11],

with subsequent studies considering a 70 cm^3 class air-cooled gasoline engine applied to a small cart [12,13]. Recent studies have continued to improve XE durability, heat transfer, and sealing performance, targeting generators, small aircraft, and range extenders for electric vehicles [13–15].

The author's research team considered that improved XE flame quenching and lubrication would make it suitable for mini combined head and power (mini-CHP) systems and started developing a three-lobe gerotor pump RE (GP3 RTE) with a customer several years ago [16,17]. We are currently conducting design and manufacturing experiments on the GP3 RTE, employing one- (1D) and three-dimensional (3D) computational fluid dynamics (CFD) to understand the stroke and flow characteristics of the engine under development, to examine related design factors' validity [18–20]. However, the 1D analysis code was mainly employed for the RE (BOOST, WAVE, GT-SUITE, etc.), and hence we needed to create the corresponding virtual reciprocating engine (VRE) model to analyze the RTE under development. Several studies have been performed for WEs using 1D analysis codes, along with a few XE studies [10,12,14,21,22]. The GP3 RTE under development and the corresponding XE were basically designed as a shape function for the GP (gerotor pump), but with a differently shaped intake and exhaust structure. Thus, we needed to develop specific VREs to analyze the corresponding GP3 RTE [14,23–25].

This study aimed to develop a 1D CFD model allowing verifiable optimization design for new RTEs. The target engine is an RTE employing the gerotor pump principle with three lobes, with intake and exhaust flow paths that change greatly as the shaft rotates. This paper reports a VRE model reflecting these unique characteristics, developed using the GT-POWER code for RE, and verifies the model's validity by comparing it to 3D CFD analysis outcomes. Conventionally, 3D designs must be changed for any factor changes to derive the optimal design factor using the 3D CFD analysis code; however, performances can be easily predicted using the 1D model, changing only the information affected by the factor change. Therefore, the VRE model introduced here provides a powerful tool to achieve optimal RE design.

2. GP3 RTE Configuration and Operation Overview

Figure 1 shows the experimental GP3 RTE layout viewed from the intake direction. The design comprises a compact engine for 5 kW class power generation, with a 336 cm^3 displacement, a 310 mm width, and a 475 mm diameter hexagonal body. There is a power shaft in the center, with the target wheel and angle sensor to measure rotational speed mounted around it. The hexagonal body is a critical part of the engine, and a spark plug is mounted on the top. The oil pump, flywheel, and exhaust pipe are installed on the other side, with an oil pan at the bottom.

Figure 2 provides a cross-sectional view of the core GP3 RTE, showing the eccentric power shaft, rotor, and housing from the center outwards. The eccentric power shaft rotates in a clockwise direction, and hence the rotor rotates in a counterclockwise direction, producing an eccentric revolution while remaining in contact with the three apex points of the housing. The external–internal gear ensures that the rotor rotates once for two power shaft rotations [24]. The rotor for the engine corresponds to an RE piston, and the shape follows an epitrochoidal function with two lobes [24]. Three lobes are arranged within the housing at 120 ° intervals, and the overall shape is determined by the outermost locus for the eccentrically rotating rotor [26]. The cavity, including the clearance volume between the rotor and the housing, corresponds to the cylinder volume (Vcy), and a combustion chamber (Vc) is provided at the upper end of each lobe. One advantage for this engine is that the combustion chamber can be installed in a fixed housing.

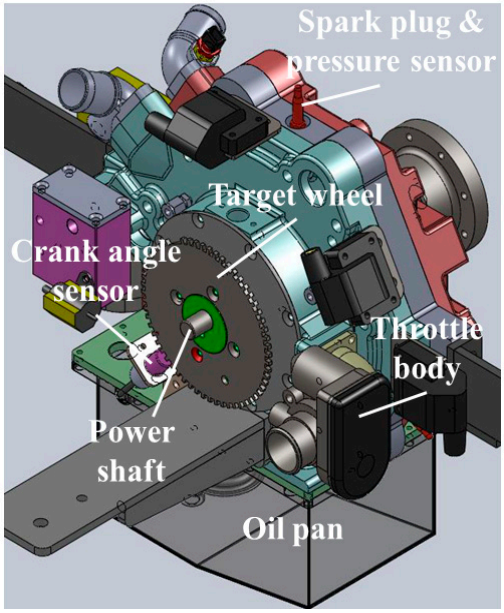

Figure 1. The GP3 engine developed in this study.

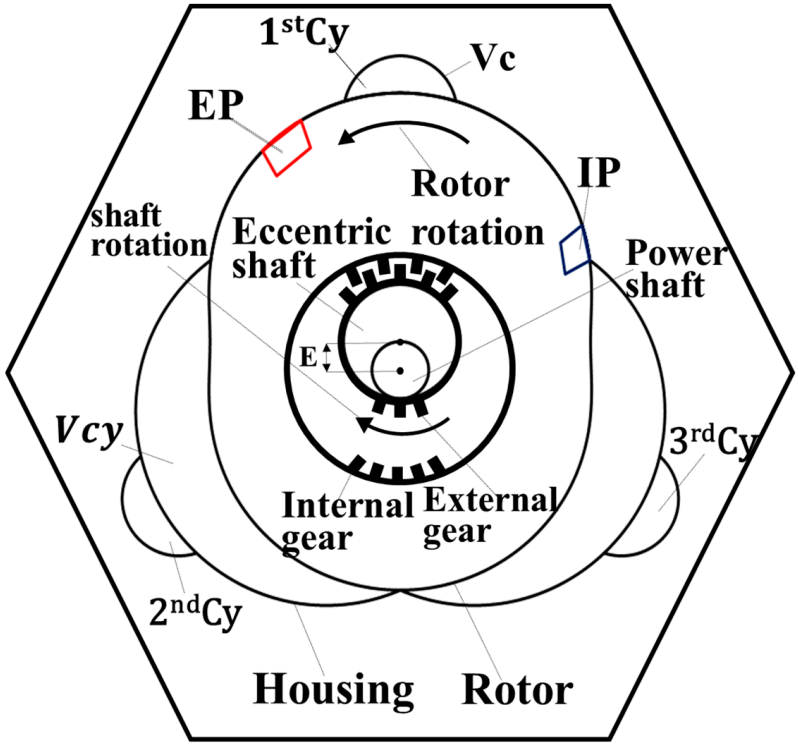

Figure 2. Core configuration for the developed GP3 engine.

Figure 3 shows the intake (IP, lower) and exhaust (EP, upper) open periods for each cylinder with respect to the power shaft rotation angle (SRA), where the stroke shown in the middle represents each stroke distribution for the first cylinder (Cy) after one cycle. The IP/EP open period corresponding to the intake/exhaust stroke is the sum of the 1/3 rotation angle (SRA = 240°) for the rotor and the port width (20°), as shown in Figure 2, due to the engine structure. Considering the first Cy, IP opens at 700° and closes at 240° past the bottom dead center (BDC) (180°), i.e., the Miller cycle, with a greater expansion ratio than the compression ratio, increasing the volumetric efficiency for the actual compression stroke. The EP opens at 540° and closes at 80° past the BDC in the next cycle. Hence, the

IP·EP overlap period is 700°–80°, and exhaust gas may be inhaled back into the cylinder through the EP (EGR) [20]. The IP·EP also has a period spanning neighboring cylinders, e.g., IP 220°–240° and EP 60°–80°. Intake/exhaust gas flow rate is determined by the effective port area (EA = (port width) × (clearance height)) rather than the geometric port area (A).

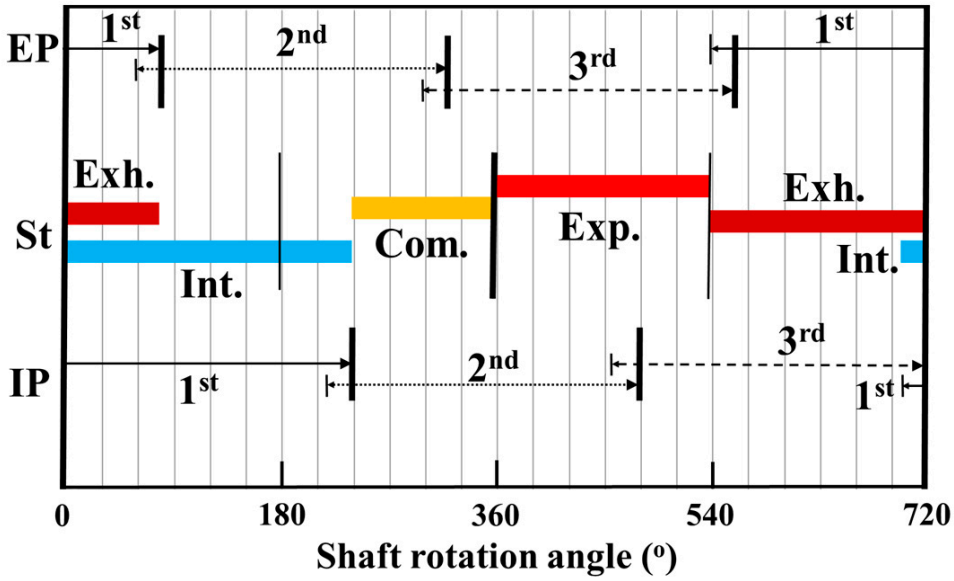

Figure 3. Port open timing and four strokes for the first cylinder.

3. VRE Modeling for GP3 RTE Analysis

3.1. GT-POWER Analysis Method

To analyze GP3 RTE using GT-POWER, which is normally exclusively employed for REs, we need to construct a VRE model that reflects the cylinder characteristics and intake and exhaust flow path behaviors for the specific engine. The equations for the conservation of mass, energy, and momentum are then analyzed for this VRE model, with the detailed analysis methods omitted here [27]. Boundary conditions were set to 550, 600, 400, and 400 K for the cylinder head, piston, and cylinder walls, respectively, based on recommended temperatures for the EngCylTWall model. The WoschniGT model, which is widely used when there is no swirl information, was employed with the minimum heat transfer coefficient Nu = 3.66 at a low RPM [28]. The combustion rate was modeled using, the SIWiebe model from the Wiebe function, which is widely used for spark ignition.

3.2. VRE Cylinder Modeling

Figure 4 shows the locus of points for the rotor and housing to obtain the GP3 RTE cylinder volume (V_{cy}) and surface area (A_{cy}). The locus of points for the rotor $R(\theta_t, \psi)$ and housing $H(\theta)$ are expressed using the link rotation mechanism with the shape factor for the eccentric distance (E) and trochoidal radius (R_T), as shown in Figure 4 [24,26]. The x and y coordinates for the locus of points for rotor Rx, Ry can be expressed as

$$R_x(\theta_t,\ \psi) = E\ cos\ (-2\psi_r) + E\ cos\ (3\theta_t + \psi) + R_T\ cos\ (\theta_t + \psi) \quad (1)$$

and

$$R_y(\theta_t,\ \psi) = E\ sin\ (-2\psi_r) + E\ sin\ (3\theta_t + \psi) + R_T\ sin\ (\theta_t + \psi) \quad (2)$$

respectively, where ψ is the rotational phase and θ_t is the outer circumferential angle for the rotor, with ψ based on the x-axis and θ_t on the long axis of the rotor.

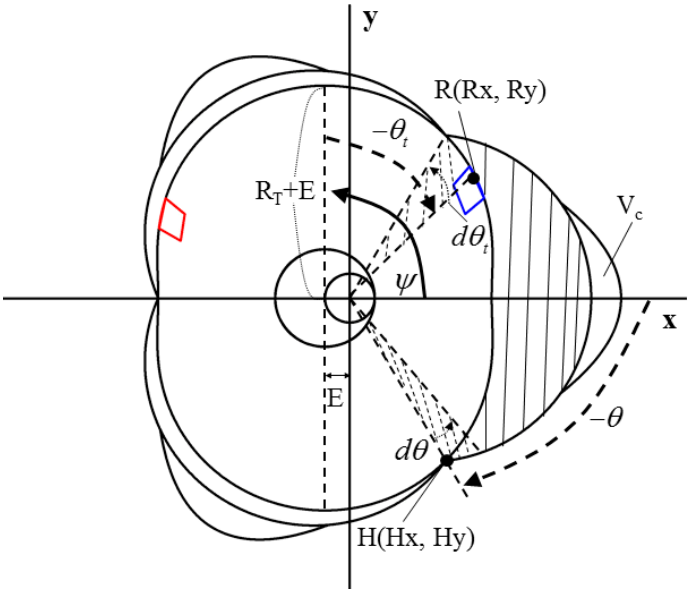

Figure 4. Locus of points for the GP3 RTE engine rotor and housing (red: EP, blue: IP).

Similarly, the locus of points for H_x, H_y can be expressed as

$$H_x(\theta) = R_T\cos(3\theta) - \frac{3E^2}{R_T}\sin(\theta)\sin(3\theta) + 2E\left\{\cos^2\frac{3\theta}{2} - \left(\frac{3\theta}{2}\right)^2\sin^2(3\theta)\right\}^{0.5}\cos(\theta) \quad (3)$$

and

$$H_y(\theta) = R_T\sin(3\theta) + \frac{3E^2}{R_T}\cos(\theta)\sin(3\theta) + 2E\left\{\cos^2\frac{3\theta}{2} - \left(\frac{3\theta}{2}\right)^2\sin^2(3\theta)\right\}^{0.5}\sin(\theta) \quad (4)$$

where θ is the outer circumferential angle for the housing in Figure 4.

Thus, cylinder volume V_{cy} is the sum of V_c over the space between the housing and the rotor,

$$V_{cy}(\psi) = Hw\left[\int_{-\pi/3}^{\pi/3}\frac{1}{2}\left\{H_x(\theta)^2 + H_y(\theta)^2\right\}d\theta - \int_{-\pi/3-\psi}^{\pi/3-\psi}\frac{1}{2}\left\{R_x(\theta_t,\psi)^2 + R_y(\theta_t,\psi)^2\right\}d\theta_t\right] + V_c \quad (5)$$

where Hw is the thickness of the housing.

Finally, cylinder surface area A_{cy} can be expressed as

$$A_{cy}(\psi) = 2\frac{V_{cy}(\psi)}{Hw} + Hw\int_{-\pi/3}^{\pi/3}\sqrt{H_x(\theta)^2 + H_y(\theta)^2}d\theta + Hw\int_{-\pi/3-\psi}^{\pi/3-\psi}\sqrt{R_x(\theta_t,\psi)^2 + R_y(\theta_t,\psi)^2}d\theta_t + A_c \quad (6)$$

where V_{cy}/Hw is the side area and A_c is the surface area of the combustion chamber.

Figure 5 shows the algorithm used to emulate the GP3 RTE cylinder and hence configure the optimal VRE cylinder. The input values include the GP3 RTE design parameters E, R_T, and Hw; GP3 RTE rotation angle θ_{SRA}; and VRE rotation angle θ_C. The volume and surface area of the GP3 RTE are calculated using (5) and (6). The bore (B) and stroke (S) of the VRE cylinder are the GP3 RTE volume and surface area, respectively, under the BDC condition (i.e., 180°). The connecting rod length of the VRE (r) is determined as follows. We can assume that r = VRE stroke, and calculate the corresponding volume and surface area for each θ_C. The surface area/volume ratio error (Er) between the VRE and GP3 RTE is then calculated for each θ_C, and summed to obtain the error for a full cycle. We repeat this process several times, extending r by 1% until r reaches 5 × VRE stroke, then define the optimal r of the VRE as the value that minimizes the cycle error.

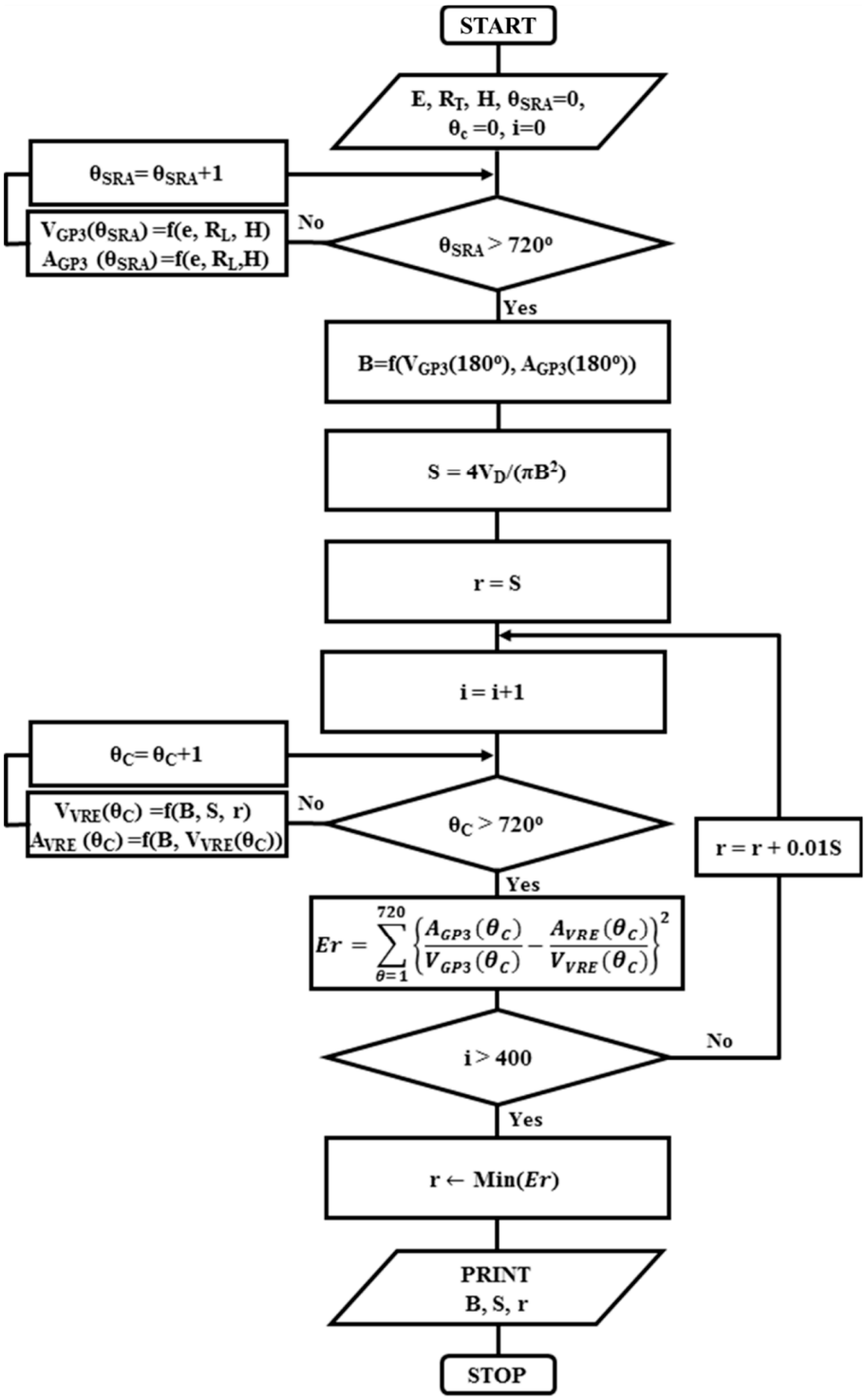

Figure 5. Flowchart to derive the VRE parameters from the GP3 RTE design and other parameters.

Table 1 shows the GP3 RTE design specifications and optimally emulated VRE specifications derived. The GP3 RTE displacement (112 × 3) is from (5) given a compression ratio = 11, V_D = 112 cm^3, and V_C = 11 cm^3. This engine is operated with an overexpansion ratio(γ) of 1.3, with an effective V_{cy} at which compression actually starts = 95 cm^3, effective compression ratio CR_E = 8.5, and CH_4 used as fuel. The GP3 RTE design parameters (E, R_T, and H) and the corresponding optimal VRE properties (B, S, and r, respectively) are shown in Table 1.

Table 1. GP3 RTE design specifications and the corresponding optimal VRE specifications.

Common Specifications	V_D	V_C	$CR(CR_E)$	γ	Fuel
	112 cm^3	11 cm^3	11 (8.5)	1.3	CH_4
GP3 RTE			VRE		
E	10 mm		B	95.71 mm	
R_T	77 mm		S	15.57 mm	
H	28 mm		r	21.90 mm	

Figure 6 compares surface area and surface-area-to-volume ratio between the GP3 RTE, VRE, and conventional square models to help establish the VRE model cylinder shape validity. The volume change with respect to the SRA was almost the same for all three engines and was omitted. Figure 6a shows that the VRE surface area is the same as for the GP3 RTE at the BDC, and only diverges by approximately 14% around the TDC condition (i.e., 360°). The surface areas of both the VRE and GP3 RTE are approximately 1.5 times that of the square model at all rotation points. Figure 6b shows that the surface-area-to-volume ratio of the VRE effectively emulates that of the GP3 RTE in most areas, except for near the TDC. In contrast, although the square engine ratio is similar to that of the GP3 RTE around the BDC, it differs by a factor ≈ 3 around the TDC. Thus, the VRE effectively emulates the GP3 cylinder volume and volume-to-surface ratio with respect to the SRA, whereas the general square engine is relatively poorly correlated with the GP3 RTE.

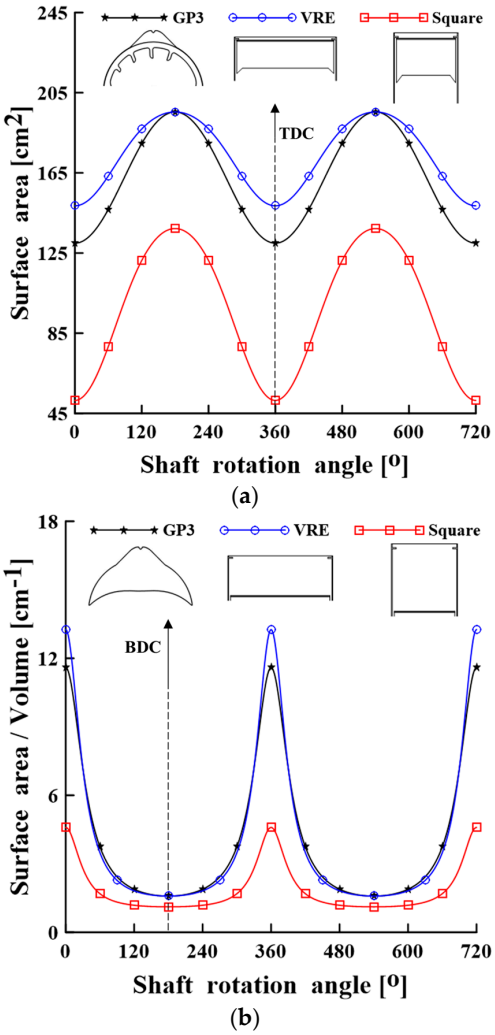

Figure 6. GP3 RTE, VRE, and square (**a**) surface area and (**b**) surface-area-to-volume ratio versus the SRA.

3.3. VRE Intake/Exhaust Flow Path Modeling and Analysis

Figure 7 shows the VRE flow path model employed. Figure 7a specifically indicates the intake (blue) and the exhaust (red) paths. Following the flow path, air is inhaled through the throttle, mixed with fuel in the mixer, introduced into the surge tank (ST) and subsequently introduced into the intake chamber (IC) of the rotor through the three intake windows (IW). The air then flows into each of the three cylinders (Cy) through the IP installed on the outer peripheral surface of the rotor. Exhaust gas is discharged into the exhaust chamber (EC) through the EP on the outer circumferential surface of the rotor in the reverse order, passes through the three exhaust windows (EW), and is finally discharged to the outside through the exhaust manifold. The flow between the IC·EC and the three cylinders occurs through the same IP and EP in an actual engine, and is achieved through the stroke distribution for each cylinder (refer to Figure 3). The effective area of the IP and EP flow path (EA_P) and the effective area of the flow path, in which the IW·EW contacts IC·EC (EA_W), changes with the rotor rotation.

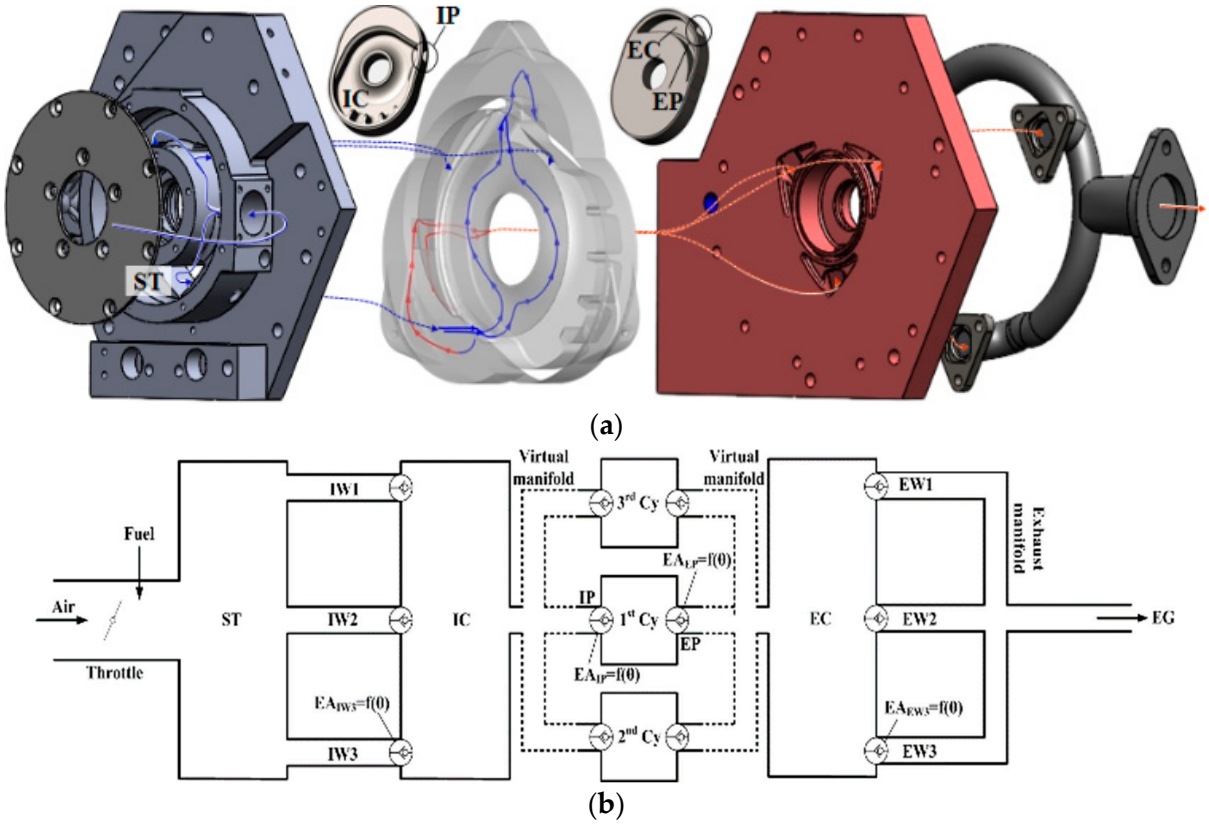

Figure 7. Intake and exhaust flow paths of (**a**) GP3 RTE core configuration and (**b**) VRE model.

Figure 7b shows the GP3 RTE flow path of the model, reflecting the intake and exhaust flow path characteristics of the actual engine. The flow path branching through IP/EP between IC·EC and the three cylinders is implemented using a virtual manifold and valve template indicated by dotted lines.

Figures 8 and 9 show flow path areas of IP·EP and IW·EW, respectively, with respect to the SRA, modeled using a valve template controlled by a function value with respect to the SRA. The figures also display the changes in the effective area (EA) with respect to the SRA of IP·EP and IW·EW.

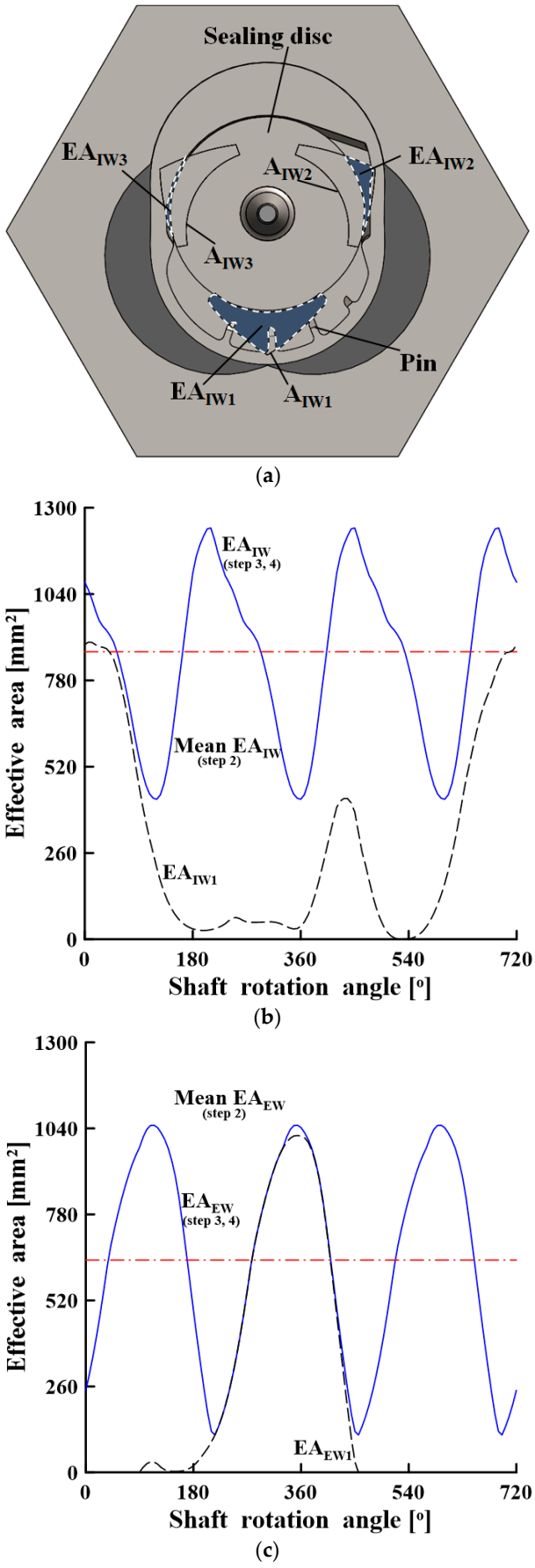

Figure 8. (**a**) Example of effective IW area (SRA = 0°), (**b**) intake, and (**c**) exhaust window areas versus the shaft rotation angle.

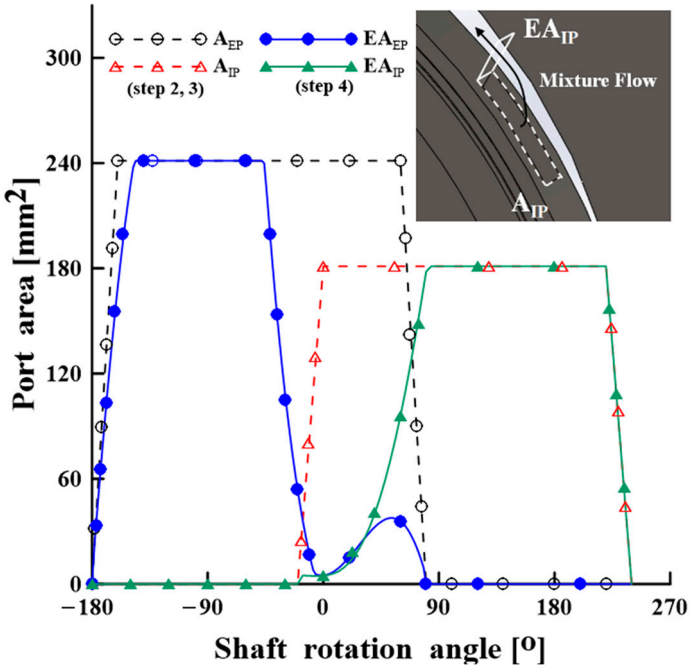

Figure 9. Comparison of the geometric open areas and effective port areas versus the SRA.

Table 2 shows the progressive VRE model steps. Step 1 is a general RE (square Cy) with the same compression ratio as that of the VRE, providing a performance reference to compare with subsequent VRE models. Step 2 is the simplest VRE model, using average IW and EW areas with respect to the SRA, and the geometric port area (A_p) of IP and EP. Step 3 reflects the changing effective area of IW·EW versus the SRA (Figure 8), and step 4 reflects effective area changes for IP·EP with respect to SRA (Figure 9). Thus, the performance sensitivity of each design factor can be separately analyzed, allowing effects from the intake/exhaust to be separated and reviewed by further subdivision.

Table 2. Model steps.

Step	Parameter		
	Cylinder	Flow Path	Valve/Port
1	Square RE	Manifold	Valve
2	VRE	Mean EA_W	A_P
3		$EA_W(\theta)$	A_P
4		$EA_W(\theta)$	$EA_P(\theta)$

Figure 8 shows the effective area (EA) of IW·EW versus the SRA of the experimental engine when applying the step 3 and 4 models. Figure 8a shows the EA_{IW} when SRA = 0°, with three fixed windows at 120° intervals, but the effective area EA_{IW} (shaded area) directly contacts the IC as the rotor rotates. Figure 8b shows EA_{IW} changes in the intake window versus the SRA. The effective area (EA_{IW1}) is first obtained (dotted line) using a design drawing for one window (IW1). The areas of the three windows are then summed considering the changes in EA_{IW2} and EA_{IW3} in the same manner as that of EA_{IW1}, maintaining 240° (SRA) phase difference. Figure 8c shows the EA_{EW} (solid line) changes versus the SRA. Similar to the case shown in Figure 8b, the EA_{EW1} of one window (dotted line) is obtained and the areas of the three windows are summed considering their phase differences.

The model for step 2 (Table 2) averages the effective area (mean EA_W) for the intake and exhaust windows (Figure 8, dash–dot line), whereas the step 3 and 4 models use the effective area versus the SRA of IW·EW (Figure 8, solid line).

Figure 9 shows the IP·EP open area versus the SRA. The geometric open area (A_P; Figure 9, dotted line) is generally regarded as the port open area. The effective area (EA_P; Figure 9, solid line) corresponds to the actual flow path, and the intake/exhaust flow rate is governed by the EA_P, defined by (port width) × (rotor-housing clearance) when the port is in close contact with the housing (Figure 9, inside corner image). These effective areas were obtained by measuring the port-housing clearance every 3° using SOLIDWORKS. Comparing the A_P and EA_P areas from Figure 9, several differences are found in the overlap period (−20° to +80°). This characteristic is unique to the GP3 RTE engine and should be considered when analyzing the engine performance. The step 2 and 3 models of A_P used the port open area, whereas step 4 used the effective area (EA_P) obtained here.

Figure 10 shows the VRE analysis map based on the flow path model from Figure 7. The flow path starts from the inlet (bottom left) and eventually reaches the outlet (bottom right), following the flow path depicted in Figure 7. The same symbols are employed in Figures 7 and 10 to identify the corresponding parts. The map assumes three VRE cylinders (marked at the center), in which the lengths and shapes of the intake and exhaust pipes are similar to those of the actual GP3 RTE. However, we excluded the throttle from the models, effectively assuming the throttle to be wide open. The three VRE models are implemented by varying the driving data of the valve actuators connected to the left and right IW·EW and IP·EP of the cylinders, as listed in Table 2.

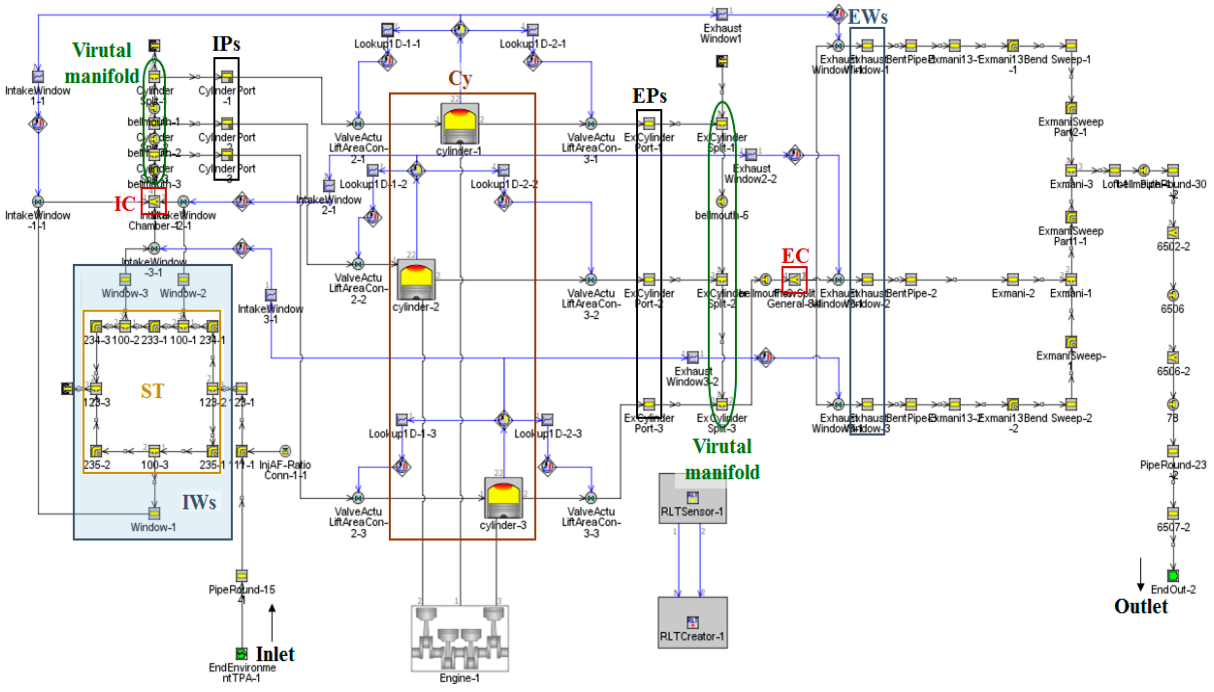

Figure 10. GT-POWER logic used for the VRE model of the GP3 RTE.

4. VRE Comparison by Step and Final Model Derivation

4.1. GT-POWER Analysis Method

Figure 11 compares the results from the four models under the same calculation conditions for each case, i.e., RPM = 3000, effective compression ratio = 8.5, and the combustion rate as the SI–Wiebe model recommended for RE analysis [28,29]. However, the VRE model reflects the Miller cycle characteristics of the GP3 RTE, which has higher filling efficiency than an RE, and hence the fuel supply is also higher [30]. Step 1 (dash–dot line) shows the general rectangular RE predicted by GT-POWER. The VRE models achieve

higher peak pressure compared to the step 1 case and reflect over-expansion; hence, these models provide reasonable results. The step 4 model (solid line) includes all the GP3 RTE characteristics of the intake and exhaust flow paths, and achieves similar results to those of 3D CONVERGE analysis.

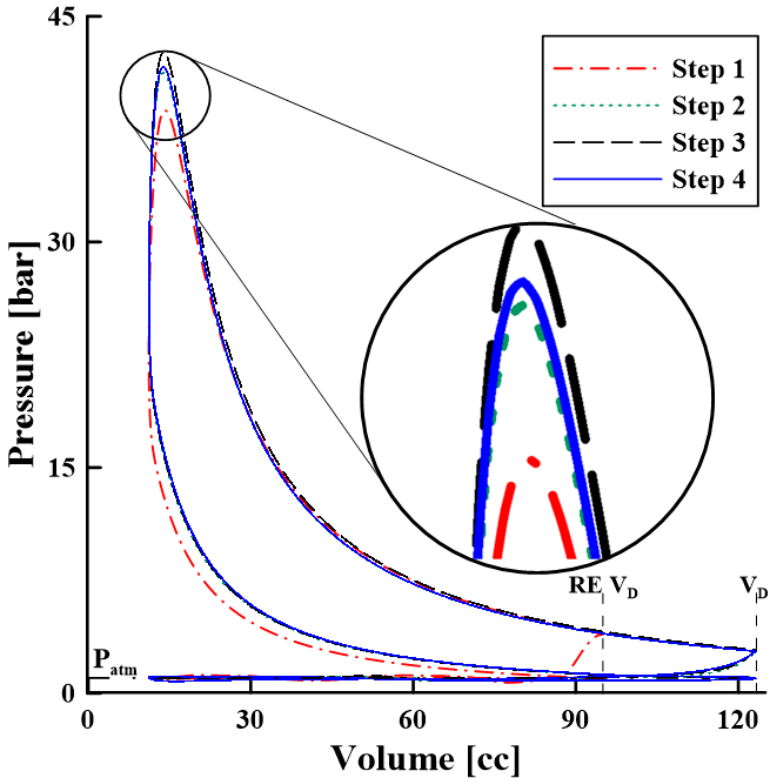

Figure 11. P-V diagrams of each step model.

The differences related to advancing the VRE model stages can be summarized as follows. Step 2 (dotted line) does not consider the changes in IW·EW and IP·EP effective area versus the SRA. Although this model predicts the basic GP3 RTE characteristics, it achieves lower performance than the step 4 model. Step 3 (dashed line) considers the effective IW·EW area changes versus the SRA, and the IW·EW area changes and port timing are harmonized. Hence, fuel intake and maximum pressure increase. Step 4 also considers the changes in the IP and EP effective area versus the SRA, and achieves a lower maximum pressure than that obtained in step 3, probably due to the reduced IP and EP effective area in the overlap region (Figure 9). Therefore, engine performance changes slightly in the different stages.

Figure 12 shows the cumulative combustion rate used for subsequent GP3 RTE analysis, derived from 3D CFD, and approximates the sigmoidal Boltzmann curve fitting. Table 3 summarizes this approximation approach, which was used for the VRE combustion model in Figure 13. The final combustion rate for this model = 0.9, which reflects the generation of a flame-quenching zone of the GP3 engine observed via CONVERGE analysis. The final combustion rate is lower than the general RE combustion rate (dash–dot line), and hence is relatively slow [20]. However, the GP3 RTE combustion rate was obtained for the first experimental engine at 3000 RPM, and subsequently applied to examine the step 4 VRE model.

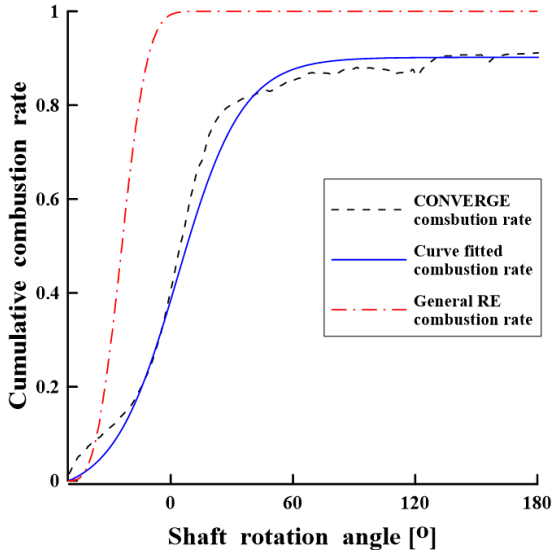

Figure 12. Cumulative combustion rate of the VRE model obtained from 3D CFD of GP3 RTE.

Table 3. Combustion rate function of the VRE model.

Equation	$y = A2+(A1-A2)\cdot 1/[1+e^{(\frac{x-x0}{dx})}]$	
Coefficient	A1	−0.03145
	A2	0.90191
	x0	3.43167
	dx	15.88452

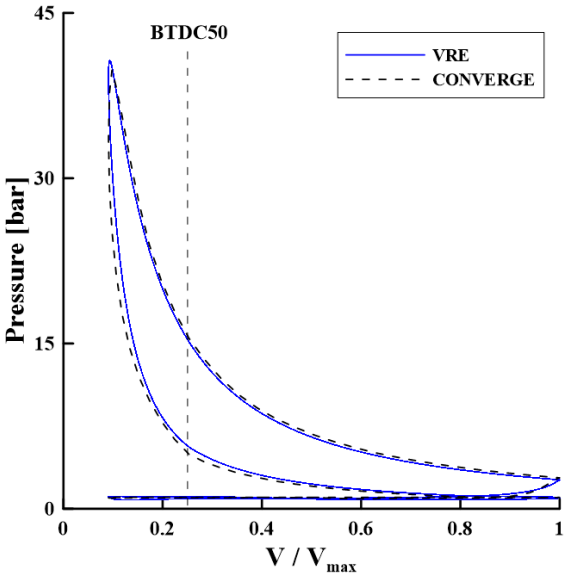

Figure 13. Typical P-V diagrams obtained from 3D CFD and the step 4 VRE model.

Figure 13 compares and verifies the analysis results from the P-V diagrams for the final VRE 1D and 3D CONVERGE models. Table 4 compares the major performance indices for these engines subsequently obtained from these analyses. The VRE model still requires the systematic review for heat transfer and combustion rate models, but provides similar P-V diagram outcomes to CONVERGE at this stage. Table 4 confirms that all the indicators provide relatively similar results. Thus, the VRE step 4 model properly predicts GP3 RTE

performance with respect to the inherent factor changes, and provides a suitable model for optimizing GP3 RTE performance.

Table 4. Performance indexes of the CONVERGE and step 4 VRE models.

	CONVERGE	Step 4 Model	Relative Error
Fuel consumption	4.2 mg/cycle	4.43 mg/cycle	−5.48%
Indicated work	4.36 kW	4.24 kW	2.75%
Efficiency	27.6%	27.1%	1.81%
EGR	16.1%	13.2%	18.01%

There is considerable inconvenience in changing the 3D design drawings for the engine whenever each factor is changed to ultimately derive optimal design factors using 3D CFD. However, using the various VRE models allows performance change tendencies to be derived with respect to factor changes without requiring the complete design to be changed. Therefore, the VRE model developed here is expected to provide a useful tool for performing engine optimization design.

4.2. VRE Model Flow Validity

Figure 14 shows GP3 RTE intake and exhaust timing, highlighting the unique flow characteristics. The effective area is represented by the IP area on the positive axis and the EP area on the negative axis. Thus, Cy 1 opening and closing for the intake and exhaust ports occur at −20° to 240° and 540° to 80°, respectively, with overlap from −20° to 80°. There are also regions at the beginning and end of the overlap region where the ports are simultaneous, and in addition at the beginning and end of the overlap region, across both cylinders, which we define as port interference. The port interference area of the experimental engine (Figure 14) confirms that the effective port flow path is relatively wide in the region of exhaust port interference (late overlap), but narrow in the region of intake port interference (early overlap). Therefore, the exhaust port interference has a significant impact on the performance of this engine. Intake–exhaust port interference is an important flow characteristic due to direct connections and interactions between the two cylinders, and must be considered carefully to accurately analyze the GP3 RTE using the VRE 1D model.

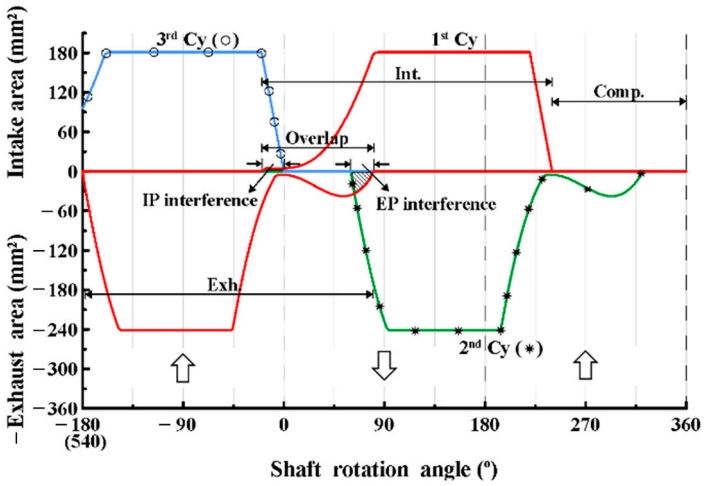

Figure 14. Intake and exhaust port timing for experimental GP3 RTE, where the solid line without symbols represents the Cy 1 effective area, * represents Cy 2, and (○) represents Cy 3; ⇑ and ⇓ indicate the rotor direction (or piston for the reciprocating motion of Cy 1).

Figure 15 shows the CONVERGE model flow with respect to the velocity vector. Cy 1 is in the intake stroke (overlap), Cy 2 is starting the exhaust stroke, and the exhaust port is open across the first and second cylinders simultaneously. Exhaust gas from Cy 2 is diverted to the exhaust chamber and the Cy 1 intake stroke, allowing the exhaust gas to enter Cy 1, acting as an EGR. This direct connection between Cy 1 and Cy 2 and the exhaust gas flow is unique to GP3 RTE, and the size of this flow directly affects EGR rate, which is believed to have a significant impact on performance. The high temperature exhaust gas is changed directly into the EGR, which will greatly affect filling efficiency.

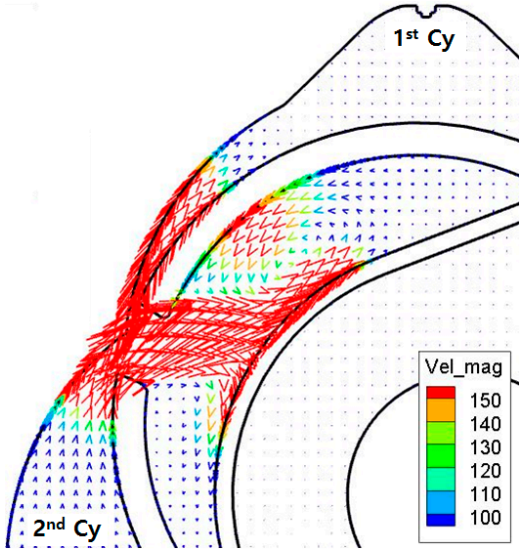

Figure 15. Flow near the exhaust port interference in the CONVERGE model.

Figure 16 shows the intake and exhaust port mass flows for the step 4 VRE 1D model to verify the inherent flow of GP3 RTE. The IP mass flow rate shows a slight reverse flow from −20° (opening the intake port), caused by the rotor direction rather than the intake port interference because the flow area of the interference zone is narrow. There is strong intake as the rotor descends; then, a reduction in mass flow through the intake port occurs from 60° to 80°, likely owing to exhaust port interference. The IP interference effects appear relatively insignificant, particularly considering the EP mass flow rate and the amount of backflow, which increases sharply in the interference region.

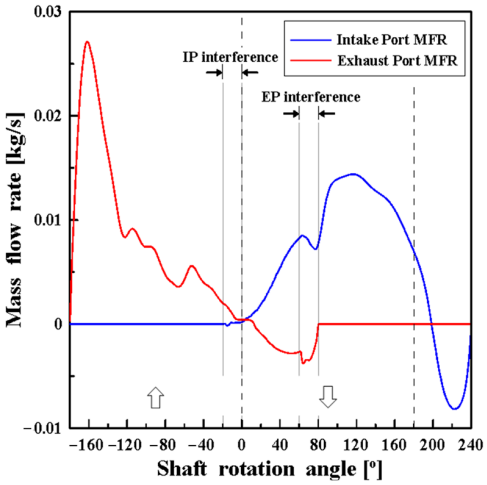

Figure 16. Mass flow rates of intake and exhaust port for the step 4 VRE 1D model: (blue) intake port mass flow, (red) exhaust port mass flow, and ⇑ ⇓ indicate the direction of rotor advance. Flow direction in a typical engine is positive (0 dashed line: TDC; 180 dashed line: BDC).

5. Optimization Using the VRE Model

5.1. Intake/Exhaust Port Location and Effective Area

Figure 17 shows the effective IP and EP areas versus the SRA. Only the port starting angles (SoI/SoE) are shown in the figure, since the ports close after a 260° starting angle due to the engine geometry. Figure 17a shows the effective area versus the SRA, where the effective area of the intake port is obtained by varying the starting angle from −80° to −20°; the maximum effective area reduces as the starting angle increases, and the effective area becomes smaller in the port interference region near the TDC (SRA = 0°). Figure 17b shows the effective area with respect to the exhaust port position. The effective exhaust port area was calculated from a starting angle of 460° to 580°, and the maximum effective area increases as the starting angle increases, and then decreases again. The effective area becomes larger in the port interference zone near the TDC (SRA = 0°). The effective areas of the intake and exhaust port converge to zero at the TDC, and the closer the port position is to the long axis of the rotor, the larger the effective area in the port interference region. Since the ports are 14 mm wide and 10° long (SRA 20°), the maximum effective area of the port is located near the start of intake (SoI) −80° and start of exhaust (SoE) 540°, where the rotor has the largest curvature.

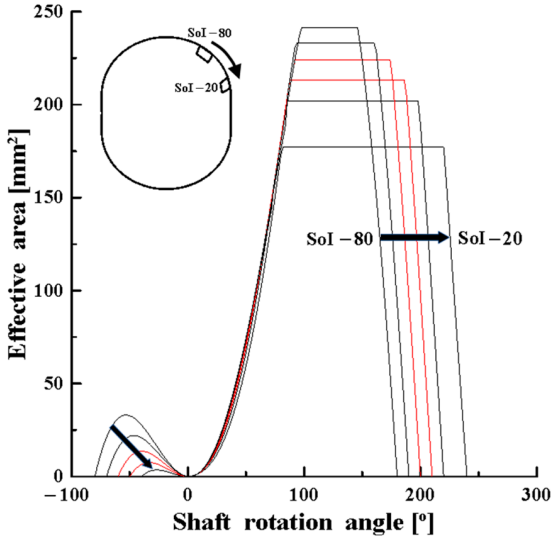

(**a**)

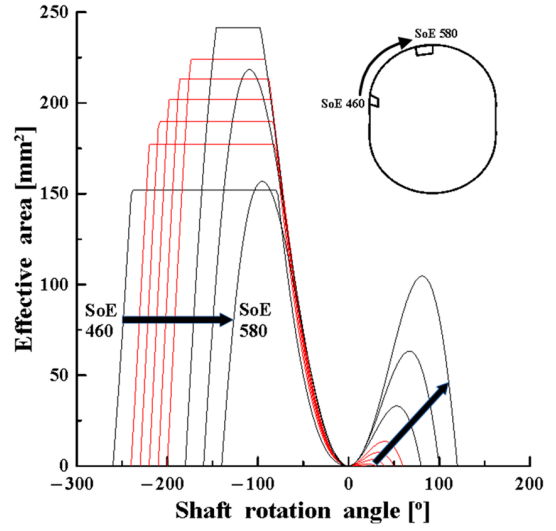

(**b**)

Figure 17. Intake/exhaust port effective areas versus the SRA, for each intake/exhaust port location. (**a**) Intake port effective areas with respect SRA. (**b**) Exhaust port effective areas versus the SRA.

The effective areas shown in Figure 17 are considered for the following simplified optimization, where the colored effective areas are those used in this study: starting angles −60° and −50° of the intake port, and 480° to 520° in 10° steps of the exhaust port. Table 5 lists the 10 cases combining the effective areas of the intake and exhaust ports.

Table 5. Main target analysis cases.

SoI	SoE				
	520°	**510°**	**500°**	**490°**	**480°**
−50°	case 1	case 2	case 3	case 4	case 5
−60°	case 6	case 7	case 8	case 9	case 10

5.2. Simple Optimization

Figure 18 shows a simple optimization to select the main cases for analysis, with the combustion rate of a typical reciprocating engine Wiebe combustion model and 3000 RPM. The maximum indicated mean effective pressure (IMEP) is achieved at SoI −50° and SoE 500° (Figure 18, ★), and the starting points of the intake and exhaust port are located between SoI −60° and −50° and SoE 480° and 520°, respectively, confirming the good performance of the IMEP. The thermal efficiency did not change significantly based on the intake and exhaust port locations, and hence is not included in Figure 18. Therefore, the main analyses were selected as 10 cases between SoI −60° to −50° and SoE 480° to 520° based on IMEP. The start angles of the intake and exhaust ports of the selected cases are shown in Table 5. It shows that cases 1 to 5 have SoI −50°, whereas cases 6 to 10 have SoI −60°, and SoE reduces as the case number increases.

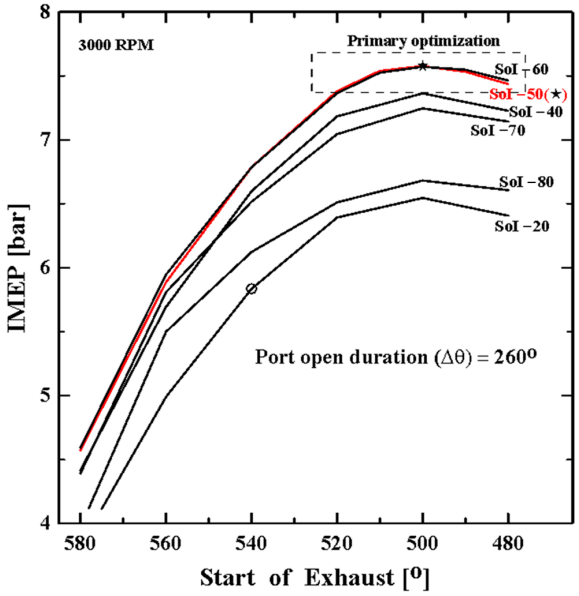

Figure 18. Primary optimization to derive the main analysis target cases: ○ shows the positions of the intake and exhaust ports of the experimental engine.

5.3. Optimizing Port Location and Operating Conditions

Figure 19 shows the results of the IMEP analysis conducted on the 10 cases (Table 5), with varying RPMs, intake and exhaust port positions, and ignition timings. The combustion rates used for this analysis were obtained from the validated 3D CFD for each RPM, at BTDC 20°. The maximum IMEP was achieved at 8.64 bar for 3000 RPM, case 8, and BTDC 0°, and the IMEP was generally high for 3000 RPM and reduced with increasing RPM. The IMEP was also high near SoI −50° and SoE 500°, achieving a high IMEP for 3000 RPM, at BTDCs 0° and 10°, and was high for 6000 RPM at BTDCs 10° and 20°.

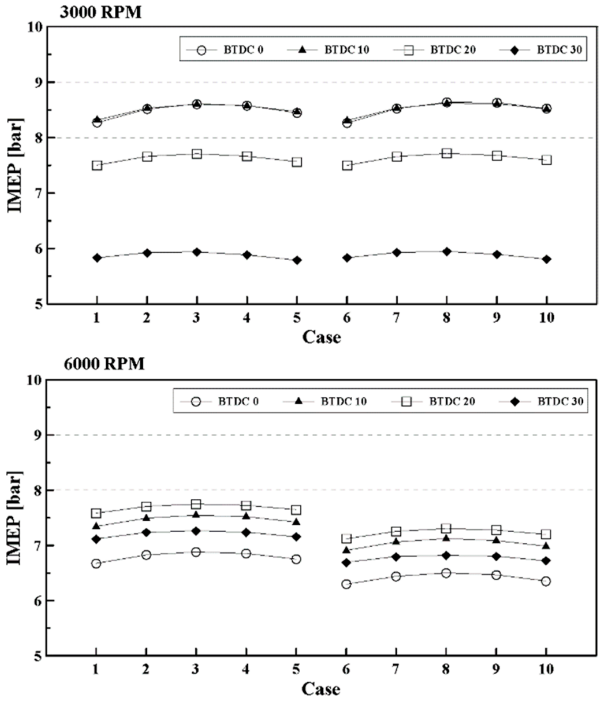

Figure 19. IMEP for each case from Table 5 at 3000/6000 RPM.

Figure 20 shows the thermal efficiency for the 10 cases listed in Table 5 at different RPM, intake and exhaust port positions, and ignition timings. The highest thermal efficiency, 37.9%, was achieved for 6000 RPM, case 1, and BTDC 20°. The thermal efficiency did not differ significantly between SoI −50° and −60° and increased with increasing SoE. It also increased with increasing RPM and was the highest overall at 6000 RPM, BTDC 10°, and 20° when ignition was timed at BTDC 20°.

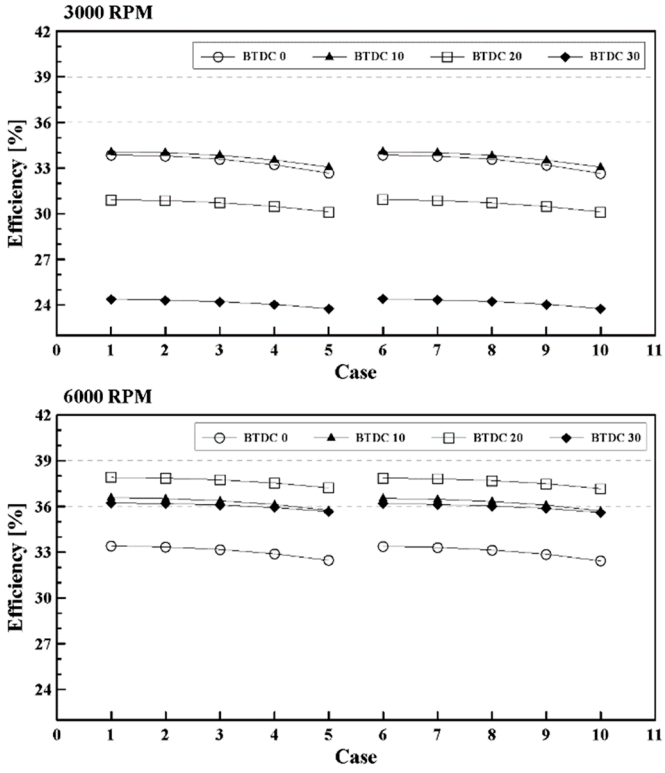

Figure 20. Efficiency corresponding to each case listed in Table 5 at 3000/6000 RPM.

6. Conclusions

This study established a VRE model that can successfully consider the engine's unique intake/exhaust windows and port effective area changes with respect to the power shaft rotation using the GT-POWER 1D CFD code for a new RTE. The VRE model validity was verified by comparing the analysis outputs with the 3D CFD results. The main outcomes can be summarized as follows.

(1) The optimum cylinder shape emulation of the VRE was achieved using the trajectory function for the rotor and housing based on the eccentric distance and trochoidal radius of GP3 RTE as the shape factors.
(2) The bore and stroke for the VRE cylinder were set such that volume and surface area were the same at the BDC, and the connecting rod length was set to minimize the surface area/volume ratio error.
(3) The VRE cylinder simulated almost the same volume and surface with respect to the SRA, and approximately 14% larger surface area/volume near the TDC.
(4) The VRE flow path model established here can reflect all the characteristics due to changing intake and exhaust windows and port effective areas unique to the GP3 RTE.
(5) The sensitivities of the unique factors of GP3 RTE were confirmed by comparing the step-wise VRE models, and subsequently analyzing the effects by subdividing the factors.
(6) The VRE step 4 model predicted almost the same engine performance indices for fuel quantity, power, efficiency, and EGR rate as those obtained from 3D CFD.
(7) The 1D model using GT-POWER adequately predicted the flow phenomena in 3D, and the developed VRE model is appropriate for optimizing GP3 RTE performance.
(8) IMEP reduced with increasing RPM, with high IMEP typically obtained for ports with SoI -50° and SoE 500°.
(9) The maximum thermal efficiency was achieved at 37.9%, 6000 RPM, case 1, and BTDC 20°. Thermal efficiency increased with increasing RPM, and slowly increased with increasing SoE.
(10) The VRE model developed here is a powerful tool for engine optimization design without changing the 3D design. Computational costs can be minimized by reducing unnecessary analysis. These advantages make this model a useful tool for performing optimization designs, such as improving the geometry of chambers and intake/exhaust windows.

Author Contributions: Conceptualization, Y.-J.P.; formal analysis, T.-J.P.; data curation, Y.-J.P.; writing—original draft preparation, Y.-J.P.; writing—review and editing, Y.-J.K.; supervision, C.-E.L.; project administration, C.-E.L. All authors have read and agreed to the published version of the manuscript.

Funding: This research was funded by Inha University Research Fund 2024.

Data Availability Statement: Data are contained within the article.

Conflicts of Interest: The authors declare no conflicts of interest.

Nomenclature

A	area (mm^2)
B	bore (mm)
CR	compression ratio
Cy	cylinder
EA	effective area (mm^2)
EC	exhaust chamber
EP	exhaust port
EW	exhaust window
GP3	gerotor pump type with three lobes
Hw	housing width (mm)

IC	intake chamber
IP	intake port
IW	intake window
r	connecting rod (mm)
RE	reciprocating engine
RTE	rotary engine
S	stroke (mm)
SoI	start of intake
SoE	start of exhaust
SRA	shaft rotation angle (degree)
ST	surge tank
V	volume (cm^3)
Vcy	cylinder volume (cm^3)
Vc	combustion chamber volume (cm^3)
Vd	displacement volume (cm^3)
VRE	virtual reciprocating engine
WE	Wankel engine
γ	over expansion ratio
θ	housing outer circumference angle (°)
θ_t	rotor outer circumference angle (°)
ψ	rotor rotation phase (°)
Subscripts	
C	clearance
E	effective
D	displacement
P	port
W	window

References

1. Wankel, F. Rotary Internal Combustion Engine. US Patent US2988065A, 13 June 1961.
2. Raju, M. *Heat Transfer and Performance Characteristics of a Dual-Ignition Wankel Engine*; SAE Technical Paper 920303; SAE International: Warrendale, PA, USA, 1992. [CrossRef]
3. Shi, C.; Chai, S.; Di, L.; Ji, C.; Ge, Y.; Wang, H. Combined experimental-numerical analysis of hydrogen as a combustion enhancer applied to Wankel engine. *Energy* **2023**, *263*, 125896. [CrossRef]
4. Bertrand, T.; Willis, E. *Rotary Engine Performance Limits Predicted by a Zero-Dimensional Model*; SAE Technical Paper 920301; SAE International: Warrendale, PA, USA, 1992. [CrossRef]
5. Spreitzer, J.; Zahradnik, F.; Geringer, B. *Implementation of a Rotary Engine (Wankel Engine) in a CFD Simulation Tool with Special Emphasis on Combustion and Flow Phenomena*; SAE Technical Paper 2015-01-0382; SAE International: Warrendale, PA, USA, 2015. [CrossRef]
6. Otchere, P.; Pan, J.; Fan, B.; Chen, W.; Lu, Y. Recent Studies of Fuels Used in Wankel Rotary Engines. *ASME J. Energy Resour. Technol.* **2021**, *143*, 030801. [CrossRef]
7. Butti, A.; Delle Site, V. *Wankel Engine for Hybrid Powertrain*; SAE Technical Paper 951769; SAE International: Warrendale, PA, USA, 1995. [CrossRef]
8. Zhang, X.; Yang, Y.; Ma, H.; Shi, M.; Wang, P. A novel diagnosis indicator for rub-impact of rotor system via energy method. *Mech. Syst. Signal Process.* **2023**, *185*, 109825. [CrossRef]
9. Shkolnik, N.; Shkolnik, A.C. Cycloid Rotor Engine. U.S. Patent US20120294747A1, 2012.
10. Leboeuf, M.; Dufault, J.; Nickerson, M.; Becker, K.; Kopache, A.; Shkolnik, N.; Shkolnik, A.; Picard, M. *Performance of a Low-Blowby Sealing System for a High Efficiency Rotary Engine*; SAE Technical Paper 2018-01-0372; SAE International: Warrendale, PA, USA, 2018. [CrossRef]
11. Shkolnik, A.; Littera, D.; Nickerson, M.; Shkolnik, N.; Cho, K. *Development of a Small Rotary SI/CI Combustion Engine*; SAE Technical Paper 2014-32-0104; SAE International: Warrendale, PA, USA, 2014. [CrossRef]
12. Littera, D.; Nickerson, M.; Kopache, A.; Machamada, G.; Sun, C.; Schramm, A.; Medeiros, N.; Becker, K.; Shkolnik, N.; Shkolnik, A. *Development of the XMv3 High Efficiency Cycloidal Engine*; SAE Paper 2015-32-0719; SAE International: Warrendale, PA, USA, 2015. [CrossRef]
13. Shkolnik, A.; Shkolnik, N.; Scarcella, J.; Nickerson, M.; Kopache, A.; Becker, K.; Bergin, M.; Spitulnik, A.; Equiluz, R.; Fagan, R.; et al. Compact, Lightweight, High Efficiency Rotary Engine for Generator, Apu, and Range-Extended Electric Vehicles. In Proceedings of the 2018 NDIA Ground Vehicle Systems Engineering and Technology Symposium Proceedings, Novi, MI, USA, 7–9 August 2018.

14. Costa, T.; Nickerson, M.; Littera, D.; Martins, J.; Shkolnik, A.; Shkolnik, N.; Brito, F. Measurement and Prediction of Heat Transfer Losses on the XMv3 Rotary Engine. *SAE Int. J. Engines* **2016**, *9*, 2368–2380. [CrossRef]
15. Nickerson, M.; Kopache, A.; Shkolnik, A.; Becker, K.; Shkolnik, N.; Bergin, M.; Spitulnik, A.; Mikhailov, K.; Equiluz, R.; Fagan, R.; et al. *Preliminary Development of a 30 kW Heavy Fueled Compression Ignition Rotary 'X' Engine with Target 45% Brake Thermal Efficiency*; SAE Technical Paper 2018-01-0885; SAE International: Warrendale, PA, USA, 2018. [CrossRef]
16. Yu, B.H.; Lee, Y.H.; Lee, C.E.; Lee, B.C.; Lee, G.G. Rotary Engine. KR Patent KR10-1813925-0000, 2015.
17. Kim, Y.-J.; Park, T.-J.; Yang, J.-H.; Lee, C.-E. Optimal Design for New Rotary Engine with Geometric Shape Functions on Combustion Chamber and Ports. *Energies* **2024**, *17*, 1754. [CrossRef]
18. Lee, C.E.; Yu, H.H.; Kim, D.H.; Park, T.J. Validation of CFD Analysis and Flow Characteristics of GP3 Rotary Engine at Motoring Condition. *J. Korean Soc. Combust.* **2020**, *25*, 11–20. [CrossRef]
19. Lee, C.E.; Kim, D.H.; Yu, H.H.; Yoon, A.S. Validation of CFD Analysis and Combustion Characteristics of GP3 Rotary Engine at Firing Condition. *J. Korean Soc. Combust.* **2020**, *25*, 21–30. [CrossRef]
20. Lee, C.E.; Park, T.J.; Park, Y.J.; Yoon, A.S. Effects of Intake·Exhaust Port Position on GP3 Rotary Engine Performances. *J. Mech. Sci. Technol.* **2020**, *44*, 717–725. [CrossRef]
21. Grabowski, L.; Pietrykowski, K.; Wendeker, M. *AVL Simulation Tools: Practical Applications*; Lublin University of Technology: Lublin, Poland, 2012.
22. Handschuh, R.F.; Owen, A.K. *Analysis of Apex Seal Friction Power Loss in Rotary Engines*; National Aeronautics and Space Administration: Cleveland, OH, USA, 2010.
23. Tartakovsky, L.; Baibikov, V.; Gutman, M.; Veinblat, M.; Reif, J. *Simulation of Wankel Engine Performance Using Commercial Software for Piston Engines*; SAE Technical Paper 2012-32-0098; SAE International: Warrendale, PA, USA, 2012. [CrossRef]
24. Colbourne, J.R. The Geometry of Trochoid Envelopes and Their Application in Rotary Pumps. *Mech. Mach. Theory* **1974**, *9*, 421–435. [CrossRef]
25. Gamez-Montero, P.J.; Codina, E. Flow Characteristics of a Trochoidal-Gear Pump Using Bond Graphs and Experimental Measurement. Part 1. *Proc. Inst. Mech. Eng. Part I J. Syst. Control. Eng.* **2007**, *221*, 331–346. [CrossRef]
26. Shung, J.B.; Pennock, G.R. Geometry for Trochoidal-Type Machines with Conjugate Envelopes. *Mech. Mach. Theory* **1994**, *29*, 25–42. [CrossRef]
27. Nabi, M.N.; Rasul, M.; Gudimetla, P. Modelling and simulation of performance and combustion characteristics of diesel engine. *Energy Procedia* **2019**, *160*, 662–669. [CrossRef]
28. Trindade, W.; Santos, R. *Combustion Modeling Applied to Engines Using a 1D Simulation Code*; SAE Technical Paper 2016-36-0347; SAE International: Warrendale, PA, USA, 2016. [CrossRef]
29. Bolehovský, O.; Novotný, J. Influence of underhood flow on engine cooling using 1-d and 3-d approach. *J. Middle Eur. Constr. Des. Cars* **2015**, *13*, 24–32. [CrossRef]
30. Martins, M.E.; Lanzanova, T.D. Full-load Miller cycle with ethanol and EGR: Potential benefits and challenges. *Appl. Therm. Eng.* **2015**, *90*, 274–285. [CrossRef]